Accepted Manuscript

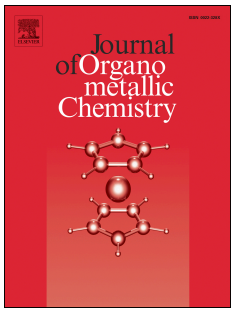

Trinuclear clusters containing 2-aminopyridinate/pyrimidinate ligands as electrocatalysts for proton reduction

Shishir Ghosh, Graeme Hogarth

PII: S0022-328X(17)30535-1

DOI: 10.1016/j.jorganchem.2017.09.015

Reference: JOM 20090

To appear in: *Journal of Organometallic Chemistry*

Received Date: 11 August 2017

Revised Date: 5 September 2017

Accepted Date: 6 September 2017

Please cite this article as: S. Ghosh, G. Hogarth, Trinuclear clusters containing 2-aminopyridinate/pyrimidinate ligands as electrocatalysts for proton reduction, *Journal of Organometallic Chemistry* (2017), doi: 10.1016/j.jorganchem.2017.09.015.

Trinuclear clusters containing 2-aminopyridinate/pyrimidinate ligands as electrocatalysts for proton reduction

Shishir Ghosh [a,b], Graeme Hogarth [b,*]

[a] *Department of Chemistry, King's College London, Britannia House, 7 Trinity Street, London SE1 1DB, UK.*

[b] *Department of Chemistry, University College London, 20 Gordon Street, London WC1H OAJ, UK*

*Email: graeme.hogarth@kcl.ac.uk (G. Hogarth)

ABSTRACT

Triiron and triruthenium clusters containing capping 2-aminopyridinate/pyrimidinate ligands are developed as functional models of the [FeFe]-hydrogenase for electrocatalytic reduction of protons to hydrogen. The 48-electron clusters $Fe_3(CO)_9(\mu_3\text{-pyNH})(\mu\text{-H})$ (**1**), $Fe_3(CO)_9(\mu_3\text{-pymNH})(\mu\text{-H})$ (**2**), $Ru_3(CO)_9(\mu_3\text{-pyNH})(\mu\text{-H})$ (**3**) and $Ru_3(CO)_9(\mu_3\text{-pymNH})(\mu\text{-H})$ (**4**) (pyNH = 2-aminopyridinate, pymNH = 2-aminopyrimidinate) are prepared from reactions of $M_3(CO)_{12}$ (M = Fe or Ru) with the corresponding heterocyclic amine at elevated temperatures. Each contains a hydride and a residual amino hydrogen in close proximity (*ca.* 2.8 Å). The triiron 2-aminopyridinate cluster **1** does not protonate by $TsOH\cdot H_2O$ (used as the proton source during catalysis), whereas its ruthenium analogue **3** undergoes slow protonation across a ruthenium-ruthenium bond. The 2-aminopyrimidinate clusters **2** and **4** undergo rapid protonation at the ring nitrogen. In MeCN, the triiron clusters show a single irreversible reduction wave (E_p = –1.61 V for **1**; E_p = –1.47 V for **2**) in the cathodic region of their CVs, while the triruthenium clusters display a pair of irreversible cathodic waves (E_p = –2.01 and –2.15 V for **1**; E_p = –1.93 and –2.09 V for **2**). All catalyze proton reduction in the presence of $TsOH\cdot H_2O$ but different mechanisms are proposed. The triiron clusters are more efficient toward proton reduction and operate at reduced overpotentials as compared to their triruthenium analogues. Introduction of a potential proton relay in these clusters neither increases the efficiency nor reduces the overpotential of catalysis which is in sharp contrast with the results observed for hydrogenase biomimetics.

Keywords: Triiron; Triruthenium; 2-Aminopyridine; 2-Aminopyrimidine; Electrocatalytic proton reduction

1. Introduction

The electrocatalytic reduction of protons is a pragmatic approach to clean H_2 production as the electrons required can be derived from renewable sources. Consequently the search for sustainable efficient base-metal electrocatalysts that are capable of catalyzing the reduction of protons to hydrogen is of great importance. The low cost, high natural abundance and biocompatibility of iron make it especially attractive and consequently iron-based complexes have come under scrutiny as potential electrocatalysts for proton reduction [1-14]. These predominantly centre on structural mimics of the active site of [FeFe]-hydrogenases (Fig. 1a) [1-4], and the proton reduction ability of non-enzyme-related iron complexes has been relatively neglected [5-14]. Low valent iron clusters are potentially promising catalysts as they often have low reduction potentials and form relatively stable anions, owing to the highly delocalised nature of the bonding within their core [3-8]. Recently a series of tri- and tetra-iron clusters containing main group element(s) including $Fe_3(CO)_9(\mu_3\text{-}S)_2$ [6,7], $Fe_3(CO)_5(\kappa^2\text{-dppv})_2(\mu_3\text{-}S)_2$ [8], $[NEt_4][Fe_4(CO)_{12}(\mu_4\text{-}N)]$ [9,10], $[NEt_4]_2[Fe_4(CO)_{12}(\mu_4\text{-}C)]$ [10], and $Fe_4(CO)_{10}(\kappa^2\text{-dppn})(\mu_4\text{-}O)$ [11] have been tested as electrocatalysts. These clusters show weak to moderate catalytic activity towards proton reduction in organic solvents in presence of proton sources. The tetra-iron clusters can also operate in water when the cation(s) are replaced with sodium [10].

In the active site of [FeFe]-hydrogenases, the diiron unit is bridged by an azadithiolate ligand with the nitrogen located in the centre of the bridge, so is flexible and can shuttle protons to and from the iron centre, being part of a proton channel that also includes four residual amino acids and a water molecule [15]. At some stage during catalysis, the active site contains an iron-bound basic hydride and a nitrogen-bound acidic proton which combine to form H_2 (Fig. 1b) [16,17]. Our strategy to design cluster-based electrocatalysts involves the inclusion of a main group electronegative element into the cluster core to facilitate interaction between such acidic and hydridic hydrogens. While sulfido- and oxo-clusters detailed earlier are catalysts for the reduction of protons to H_2, the main group element plays a passive role and is not directly involved in the catalysis [11]. We have thus turned our attention to clusters

which already contain acidic and hydridic hydrogens in close proximity. Triiron 2-aminopyridinate-capped clusters are ideal candidates for this as they contain a metal-bound basic hydride and nitrogen-bound acidic (relatively) hydrogen in close proximity (Fig. 1c). Unlike in the enzyme's active site, the bridging nitrogen in these clusters is rigid, so to facilitate interaction between acidic and hydridic hydrogen they must undergo structural rearrangement which may be achieved after reduction.

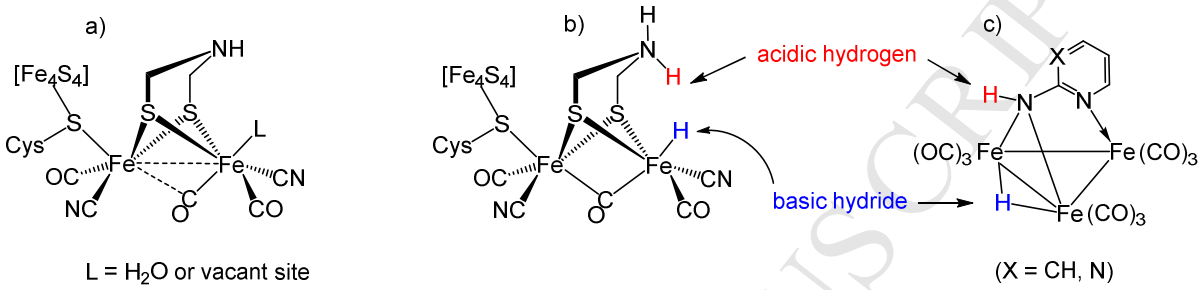

Fig. 1 - (a) The active site of the [FeFe]-hydrogenase enzyme, (b) proposed hydride-proton interaction at the active site of [FeFe]-hydrogenase enzyme during catalysis, (c) $Fe_3(CO)_9(\mu_3\text{-}L)(\mu\text{-}H)$ (L = 2-aminopyridinate, 2-aminopyrimidinate) as functional models active site.

2. Results and discussion

2.1. Synthesis and structure

Cabeza and co-workers have previously investigated the reactivity of 2-aminopyridinates/pyrimidinates towards low-valent ruthenium and osmium clusters, but no attempts have been made to prepare their iron analogues [18,19]. We prepared the triiron clusters $Fe_3(CO)_9(\mu_3\text{-pyNH})(\mu\text{-H})$ (**1**) and $Fe_3(CO)_9(\mu_3\text{-pymNH})(\mu\text{-H})$ (**2**), the latter containing an extra nitrogen atom within the heterocyclic ring, in order to investigate their electrocatalytic activity toward proton reduction. While the bridging nitrogen in both clusters is saturated, the free lone pair on the ring nitrogen in the latter can readily bind with a proton and may transfer it to the cluster core during catalysis akin to the bridgehead nitrogen in the active site. Clusters **1** and **2** were prepared upon reaction of $Fe_3(CO)_{12}$ with the corresponding heterocyclic amine at 80 °C (Scheme 1). Yields were low (4% for **1** and 8% for **2**) and attempts to improve these by changing the solvent and reaction conditions were unsuccessful. Treatment of $Fe_3(CO)_{12}$ with two molar equivalents of 2-aminopyridine/pyrimidine in boiling

benzene for 1 h afforded **1** and **2** in optimal yields. Both are air-stable in the solid-state but decompose slowly in solution when exposed to air.

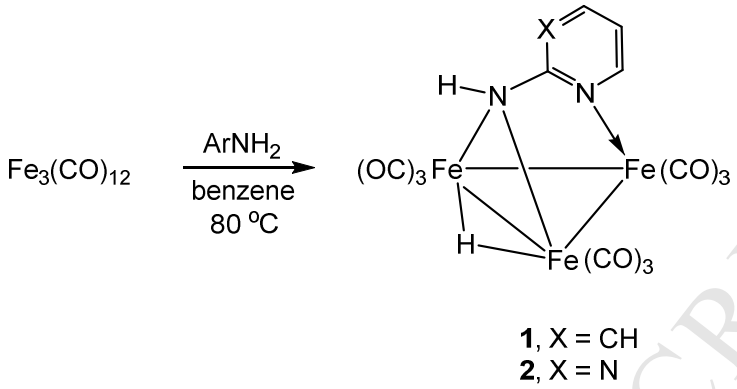

Scheme 1. Synthesis of **1-2**.

Clusters **1-2** have been characterized by spectroscopic and analytical data together with a single crystal X-ray diffraction study for **2**. In the ^{1}H NMR spectra, each displays a high-field singlet (δ –12.66 and –12.65 ppm for **1** and **2** respectively) attributed to the bridging hydride in addition to resonances for the heterocyclic ring protons in the aromatic region. The molecular structure of **2** is depicted in Fig. 2, with the caption containing selected bond lengths and angles. The molecule consists of a triiron core ligated by a face-capping 2-aminopyrimidinate (pymNH) ligand, and nine carbonyls equally distributed over three iron atoms. A hydride was located from a difference map and spans across the same Fe─Fe edge that is symmetrically bridged by the exocyclic nitrogen of the capping ligand [Fe(2)─N(1) 1.971(2), Fe(3)─N(1) 1.978(1) Å]. This edge [Fe(2)─Fe(3) 2.5223(7) Å] is significantly shorter (*ca.* 0.1 Å) than the others [Fe(1)─Fe(2) 2.6113(7), Fe(1)─Fe(3) 2.5999(8) Å] probably as a consequence of the amide bridge. The pymNH ligand is also bonded to the remote iron through one of the ring nitrogen atoms and lies almost perpendicular to the metallic plane. The hydride ligand resides on the opposite face of the metallic plane with respect to the pymNH ligand and the non-bonding distance between the hydride and the amino-hydrogen is 2.809 Å.

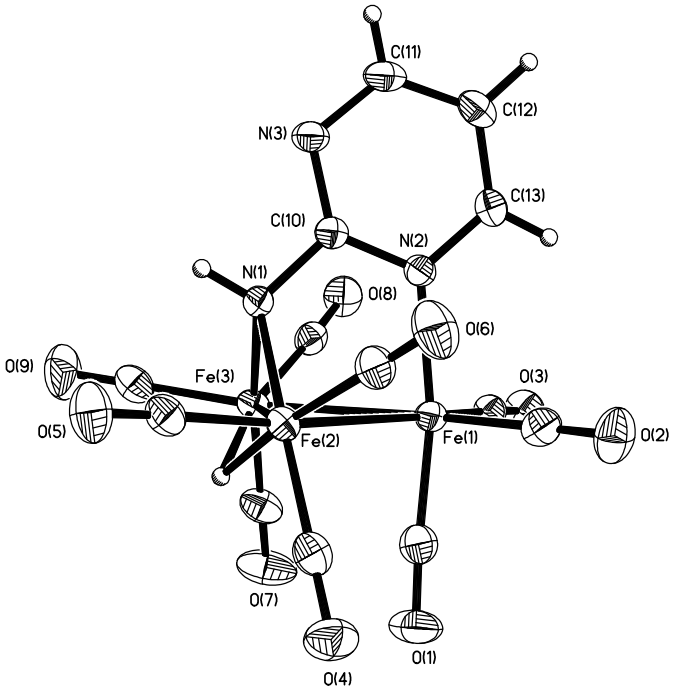

Fig. 2. ORTEP diagram of the molecular structure of $Fe_3(CO)_9(\mu_3\text{-pymNH})(\mu\text{-H})$ (**2**), showing 50% probability thermal ellipsoids. Selected bond distances [Å] and angles [º]: Fe(1)─Fe(2) 2.6113(7), Fe(2)─Fe(3) 2.5223(7), Fe(1)─Fe(3) 2.5999(8), Fe(1)─N(2) 1.9974(2), Fe(2)─N(1) 1.971(2), Fe(3)─N(1) 1.978(1), Fe(2)─N(2)─Fe(3) 79.39(7), N(1)─Fe(2)─Fe(3) 50.44(6), N(1)─Fe(3)─Fe(2) 50.17(6), N(1)─Fe(2)─Fe(1) 76.67(6), N(2)─Fe(1)─Fe(2) 84.36(6), Fe(1)─Fe(2)─Fe(3) 60.82(6), Fe(3)─Fe(1)─Fe(2) 57.898(2), Fe(2)─Fe(3)─Fe(1) 61.280(2).

It is well-known that heavier transition metal clusters show greater stability as compared to their first row analogues due to relatively stronger metal-metal bonds [20] which can allow the identification of reaction intermediates. In this way valuable information about the mechanism, as well as various kinetic and thermodynamic parameters, can be obtained. With this in mind we also examined the ruthenium clusters $Ru_3(CO)_9(\mu_3\text{-pyNH})(\mu\text{-H})$ (**3**) [18c] and $Ru_3(CO)_9(\mu_3\text{-pymNH})(\mu\text{-H})$ (**4**) [18b] which were prepared following a similar method reported by Cabeza and co-workers (Scheme 2). Yields are higher (33% for **3** and 41% for **4**) possibly as a consequence of relatively strong ruthenium-ruthenium bonds. Both **3** and **4** were previously characterized only by spectroscopic data [18b-c]. We were able to grow single crystals and carried out X-ray diffraction analysis, the results of which are shown in Figs. 3 and 4.

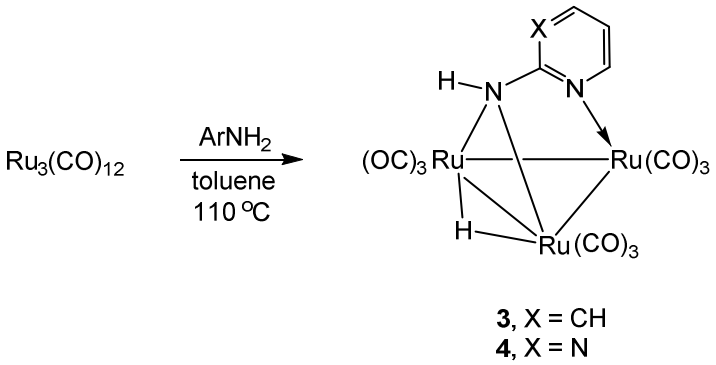

Scheme 2 - Synthesis of **3**-**4** [18b-c].

Structures of **3** and **4** are similar to that of **2** and the related triruthenium complex $Ru_3(CO)_9(\mu_3\text{-pyNPh})(\mu\text{-H})$ [18c]. The hydride ligand was located from a difference map and spans across the longest Ru–Ru vector [Ru(2)─Ru(3) 2.7556(5) Å in **3** and Ru(1)─Ru(2) 2.7532(4) Å in **4**], which is also symmetrically bridged by the exocyclic nitrogen of the heterocyclic amine [Ru(2)─N(2) 2.119(2) and Ru(3)─N(2) 2.119(2) Å in **3**; Ru(1)─N(1) 2.123(2) and Ru(2)─N(1) 2.128(2) Å in **4**]. This is in contrast with **2** in which the Fe–Fe vector simultaneously bridged by 2-aminopyrimidinate and hydride is the shortest edge. The face-capping heterocyclic amine lies almost perpendicular to the metallic plane by coordinating to the third ruthenium using (one of) the ring nitrogen(s). Akin to **2**, the bridging hydride is located on the opposite face of the metallic plane with respect to the heterocyclic amine and the non-bonding distance between the hydride and amino nitrogen is 2.834 Å in **3** and 2.873 Å in **4**.

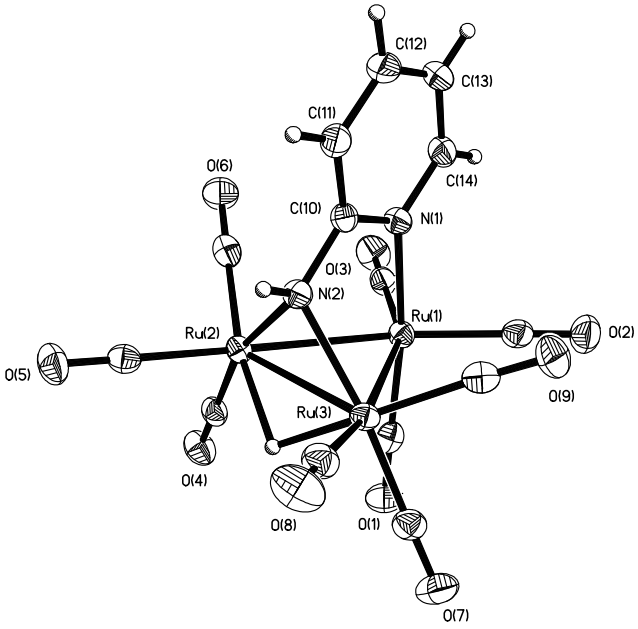

Fig. 3 - ORTEP diagram of the molecular structure of $Ru_3(CO)_9(\mu_3\text{-pyNH})(\mu\text{-H})$ (**3**), showing 50% probability thermal ellipsoids. Selected bond distances [Å] and angles [º]: Ru(1)─Ru(2) 2.7261(5), Ru(2)─Ru(3) 2.7556(5), Ru(1)─Ru(3) 2.7289(6), Ru(1)─N(1) 2.142(2), Ru(2)─N(2) 2.119(2), Ru(3)─N(2) 2.119(2), N(1)─Ru(1)─Ru(2) 83.31(6), N(1)─Ru(1)─Ru(3) 84.02(6), Ru(2)─N(2)─Ru(3) 81.10(7), N(2)─Ru(2)─Ru(3) 49.45(6), N(2)─Ru(3)─Ru(2) 49.45(6), Ru(1)─Ru(2)─Ru(3) 59.710(14), Ru(3)─Ru(1)─Ru(2) 60.683(12), Ru(2)─Ru(3)─Ru(1) 59.607(9), C(4)─Ru(2)─Ru(3) 116.33(8), C(5)─Ru(2)─Ru(3) 112.82(8), C(7)─Ru(3)─Ru(2) 117.71(8), C(8)─Ru(3)─Ru(2) 112.77(8).

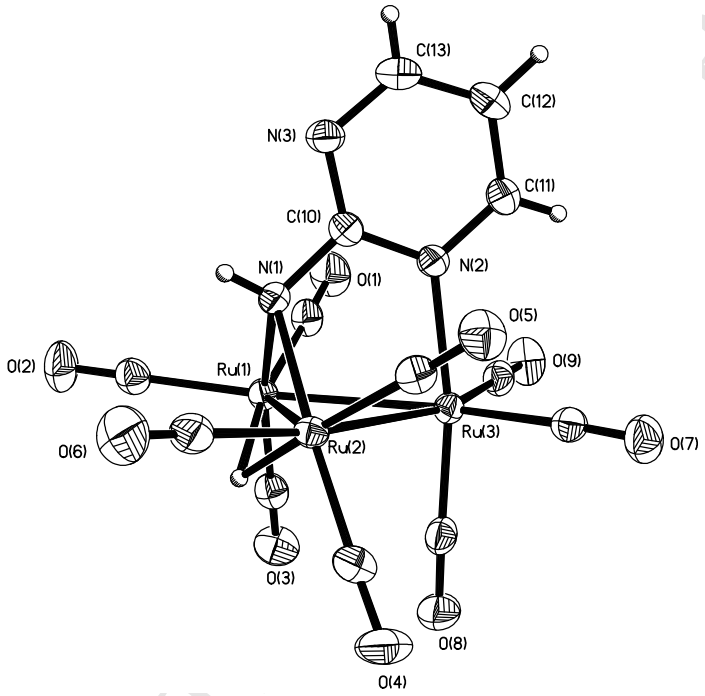

Fig. 4 - ORTEP diagram of the molecular structure of $Ru_3(CO)_9(\mu_3\text{-pymNH})(\mu\text{-H})$ (**4**), showing 50% probability thermal ellipsoids. Selected bond distances [Å] and angles [º]: Ru(1)─Ru(2) 2.7532(4), Ru(2)─Ru(3) 2.7248(5), Ru(1)─Ru(3) 2.7303(5), Ru(3)─N(2) 2.136(2), Ru(1)─N(1) 2.123(2), Ru(2)─N(1) 2.128(2), N(2)─Ru(3)─Ru(1) 83.29(6), N(2)─Ru(3)─Ru(2) 84.01(5), Ru(1)─N(1)─Ru(2) 80.73(8), N(1)─Ru(1)─Ru(2) 49.71(6), N(1)─Ru(2)─Ru(1) 49.57(6), Ru(1)─Ru(2)─Ru(3) 59.786(9), Ru(3)─Ru(1)─Ru(2) 59.590(14), Ru(2)─Ru(3)─Ru(1) 60.624(9), C(3)─Ru(1)─Ru(2) 116.64(8), C(2)─Ru(1)─Ru(2) 114.06(8), C(4)─Ru(2)─Ru(1) 117.00(8), C(6)─Ru(2)─Ru(1) 113.52(8).

2.2. Electrochemistry

The electrochemical responses of **1**-**4** were studied in MeCN by cyclic voltammetry (CV). Triiron clusters **1**-**2** exhibit single irreversible reduction and oxidation waves (Fig. 5 and Table 1) at a scan rate of 0.1 Vs^{-1}, the reversibility of which does not improve when the

scan rate is varied (Figs. S1 and S2). Thus, the radical ions of these clusters are unstable in MeCN over the lifetime of the CV experiment, which probably undergo solvolysis after reduction/oxidation. The 2-aminopyrimidinate cluster **2** reduces at ca. 140 mV more positive than **1** showing that the reduction potential of these clusters can be tuned by modifying the pyridinate ring. Consequently, cluster **2** is oxidized at a ca. 90 mV more positive as compared to **1** (Table 1). CVs of both clusters also show a series of small oxidative features on the return scan (*ca.* between –1.4 and 0 V) due to the oxidation of products formed during their irreversible reduction. The current function ($i_p/\sqrt{v}$) associated with the reduction of **1** and **2** shows slight deviation from linearity at slow scan rates (Fig. S3), which indicates that more than one electron may be involved in the electrode process on longer time scales.

Table 1 - Redox potentials for **1**-**4**.

Compounds	E_p^{red1} / V	E_p^{red2} / V	E_p^{ox1} / V	E_p^{ox2} / V
$Fe_3(CO)_9(\mu_3\text{-pyNH})(\mu\text{-H})$ (**1**)	–1.61	–	0.26	–
$Fe_3(CO)_9(\mu_3\text{-pymNH})(\mu\text{-H})$ (**2**)	–1.47	–	0.35	–
$Ru_3(CO)_9(\mu_3\text{-pyNH})(\mu\text{-H})$ (**3**)	–2.01	–2.15	0.08	0.31
$Ru_3(CO)_9(\mu_3\text{-pymNH})(\mu\text{-H})$ (**4**)	–1.93	–2.09	0.24	0.45

The triruthenium clusters undergo two closely spaced irreversible reductions in the cathodic region (Fig. 6) with the pyrimidinate cluster **4** reducing at 80 mV more positive potential as compared to the pyridinate cluster **3** (Table 1). Both also exhibit two irreversible oxidation waves in the anodic region. No significant change was observed when the scan rate was varied (Figs. S4 and S5). A series of oxidative features have also seen in their CVs on the return scan (*ca.* between –1.4 and 0 V), which are associated with their irreversible reduction. The current function associated with the first reduction of **3** and **4** also deviates slightly from linearity at very slow scan rates (Fig. S3).

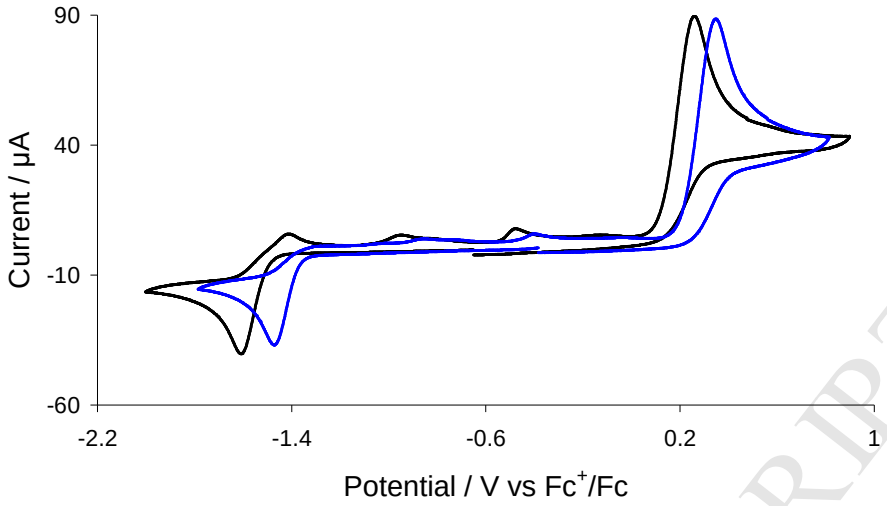

Fig. 5 - CVs of $Fe_3(CO)_9(\mu_3\text{-pyNH})(\mu\text{-H})$ (**1**) (black) and $Fe_3(CO)_9(\mu_3\text{-pymNH})(\mu\text{-H})$ (**2**) (blue) in MeCN (1 mM solution, supporting electrolyte $[NBu_4][PF_6]$, scan rate 0.1 Vs^{-1}, glassy carbon electrode, potential vs Fc^+/Fc).

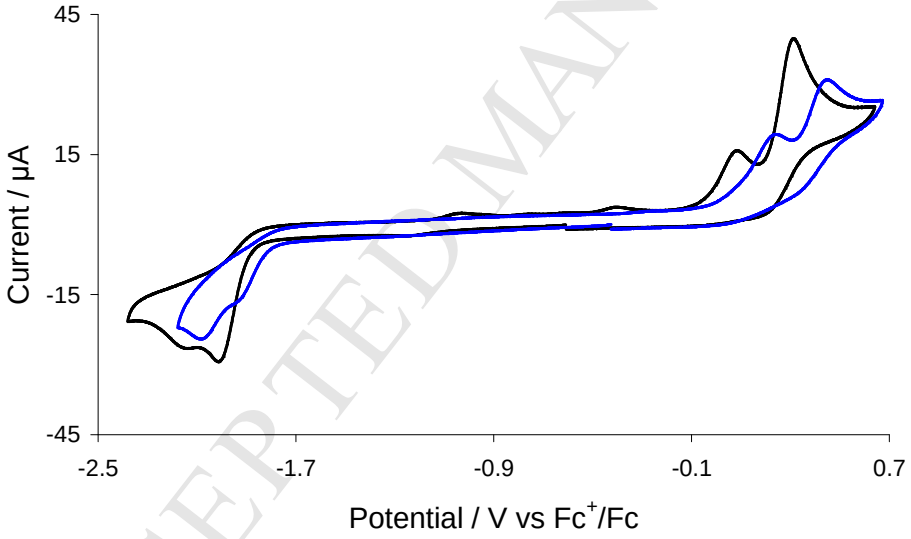

Fig. 6 - CVs of $Ru_3(CO)_9(\mu_3\text{-pyNH})(\mu\text{-H})$ (**3**) (black) and $Ru_3(CO)_9(\mu_3\text{-pymNH})(\mu\text{-H})$ (**4**) (blue) in MeCN (1 mM solution, supporting electrolyte $[NBu_4][PF_6]$, scan rate 0.1 Vs^{-1}, glassy carbon electrode, potential vs Fc^+/Fc).

2.3. Reactions with acids

The protonation behaviour of **1**-**4** was investigated in MeCN and/or CH_2Cl_2 by adding $TsOH\cdot H_2O$ ($pK_a \approx 8.5$ in MeCN) [21] and $HBF_4\cdot Et_2O$ ($pK_a \approx 0.1$ in MeCN) [21]. Cluster **1** is not protonated by $TsOH\cdot H_2O$, and decomposes rapidly in the presence of $HBF_4\cdot Et_2O$. Although **1** has two free Fe─Fe edge for protonation, it most probably does not accommodate

the incoming proton along these edges. We suggest that $HBF_4 \cdot Et_2O$ protonates one of the Fe─N bonds between the cluster core and exocyclic nitrogen thus breaking the nitrogen bridge which leads to decomposition. Protonation of **2** is expected to occur either at the unbound nitrogen of the pyrimidine ring or across one of the non-bridged Fe─Fe vectors, events that can be easily differentiated by IR spectroscopy. Addition of one molar equivalent of $HBF_4 \cdot Et_2O$ to a CH_2Cl_2 solution of **2** leads to partial protonation of the cluster. Two new absorption bands appear at 2086 and 2054 cm^{-1} in addition to the absorption bands displayed by the neutral cluster. The intensity of the new bands was seen to decline slowly and the original spectrum recovered after 1 h (Fig. S6). Since $HBF_4 \cdot Et_2O$ is volatile, it evaporates thus shifting the protonation equilibrium toward left which accounts for the regeneration of neutral **2**. The small blue shift of the highest energy absorption band (ca. 12 cm^{-1}) indicates that the proton is located at the pyrimidine ring. The reversibility of this process was also tested in MeCN (the solvent used for catalysis) by adding pyridine into a protonated solution of **2**. Again the original spectrum was recovered upon addition of equivalent amount of pyridine indicating that protonation at the free ring nitrogen of pymNH ligand is fully reversible (Fig. S7). When a slight excess of $HBF_4 \cdot Et_2O$ (3 equivalents) was added to this solution, complete protonation at pyrimidine ring nitrogen was observed and the carbonyl absorption bands of **2** were clearly replaced by a new set of absorptions at 2086, 2054, 2031, 2006 and 1995 cm^{-1} (Figs. S8 and S9). However, the gradual decrease of peak intensity over time indicates that $\mathbf{2H^+}$ also decomposes slowly in presence of air (Fig. S9).

Protonation of **2** was monitored by ^1H NMR spectroscopy in CD_3CN. Fig. 7 shows the hydride region of the spectrum recorded before and after addition of 3 molar equivalents of $HBF_4 \cdot Et_2O$ as a function of time. Upon addition of acid, two new hydride resonances appeared at δ –9.62 and –9.66 ppm at the expense of the resonance attributed to the neutral complex at δ –12.66 ppm. We suggest that the appearance of two new hydride resonances is due to the presence of two different isomers of $\mathbf{2H^+}$ as shown in Scheme 3. Although in **2** the hydride is static and resides across the Fe─Fe edge bridged by the exocyclic nitrogen of heterocyclic amine, we suggest that it moves across all three Fe─Fe edges in solution after protonation at the free ring nitrogen. This explains the appearance of two new hydride resonances upon addition of acid in to **2**. The aromatic region of the spectrum is not very informative, but it shows new resonances for $\mathbf{2H^+}$ in addition to those of the parent cluster **2**. A new broad singlet also appeared at δ 10.47 after addition of acid which faded with other

aromatic resonances associated with $\mathbf{2H}^+$ and is attributed to the incoming proton bound to the nitrogen of the pyrimidine ring (Fig. S10).

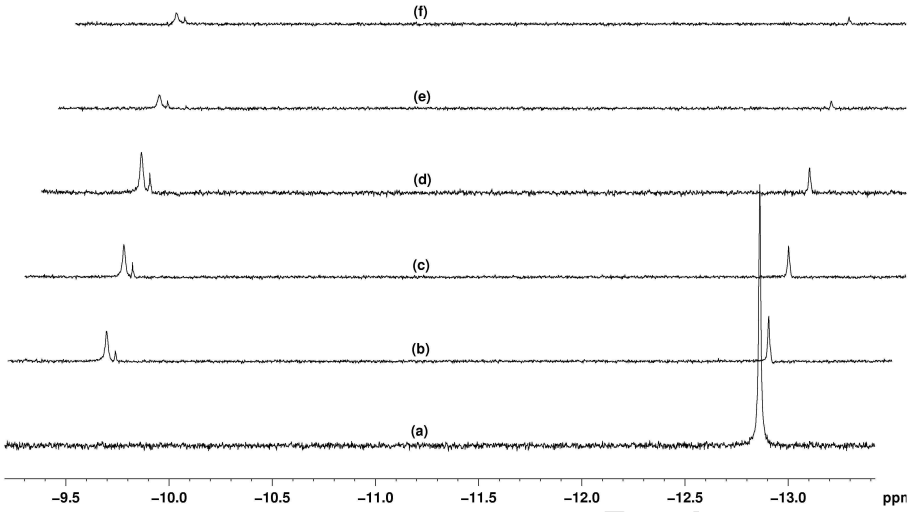

Fig. 7 - Hydride region of the ^{1}H NMR spectrum of **2** in CD_3CN – (a) in the absence of acid, (b) after addition of 3 molar equivalents of $HBF_4 \cdot Et_2O$, (c) after 10 min of acid addition, (d) after 30 min of acid addition, (e) after 90 min of acid addition and (f) after 2 h of acid addition.

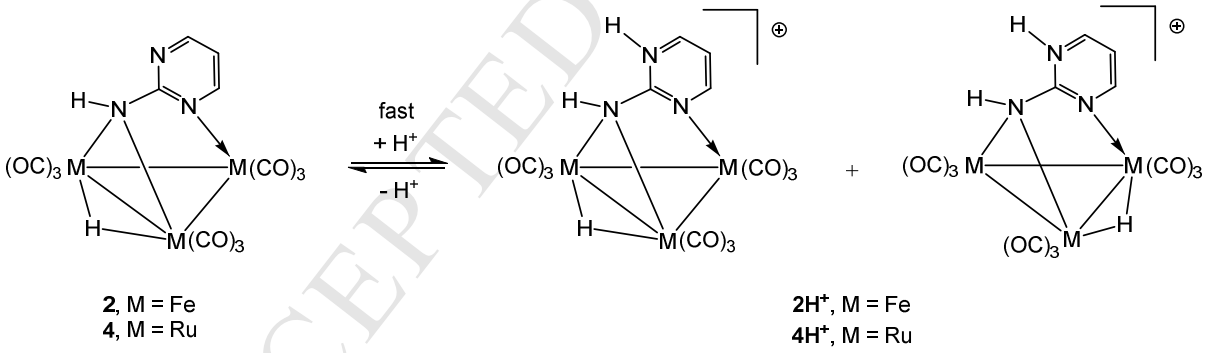

Scheme 3 - Protonation of $M_3(CO)_9(\mu_3\text{-pymNH})(\mu\text{-H})$ (M = Fe, Ru).

Addition of $HBF_4 \cdot Et_2O$ into a CH_2Cl_2 solution of **3** and **4** resulted in the formation of cloudy suspensions, so their protonation behaviour was investigated in MeCN using $TsOH \cdot H_2O$ as the proton source. Unlike **1**, which is not protonated by $TsOH \cdot H_2O$, the ruthenium analogue **3** reacts slowly with $TsOH \cdot H_2O$ in MeCN to form $\mathbf{3H}^+$ owing to the greater basicity of the triruthenium core. Upon addition of 3 molar equivalent of $TsOH \cdot H_2O$ two relatively weak new absorptions were observed at 2121 and 2102 cm^{-1} with complete

protonation occurring over 30 min. Protonated **3H**$^+$ displays absorptions at 2121m, 2102m, 2072vs, 2033vs, 2007vs, 1994 vs cm^{-1} (Fig. S11) and the ~ 40 cm^{-1} blue shift of the highest energy absorption band suggests protonation across a Ru–Ru vector. Cabeza and co-workers studied the protonation of $Ru_3(CO)_9(\mu_3$-MepyNH)(μ-H) (MypyNH = 2-amino-6-methylpyridinate) which was also found to protonate across a Ru–Ru vector akin to **3** and the structure of $[Ru_3(CO)_9(\mu_3$-MepyNH)(μ-H)$_2][BF_4]$ was established both in solution and in the solid-state [18d-e]. The hydride resonance of **3** at δ –11.60 ppm was replaced by a new singlets at δ –12.39 ppm indicating that both hydrides in **3H**$^+$ move rapidly across the Ru–Ru vectors becoming equivalent on the NMR timescale (Scheme 4).

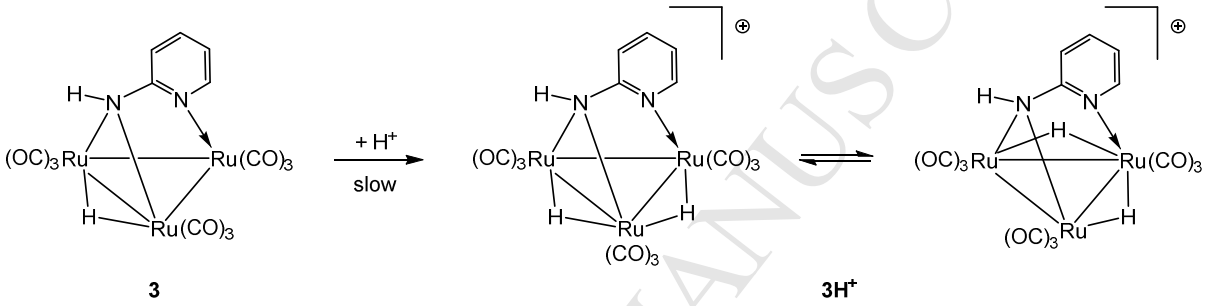

Scheme 4 - Protonation of $Ru_3(CO)_9(\mu_3$-pyNH)(μ-H) (**3**).

Akin to **2**, cluster **4** protonates rapidly at the free ring nitrogen of the pymNH ligand in MeCN upon addition of 3 molar equivalent of TsOH·H_2O. The highest energy absorption band shows only *ca.* 11 cm^{-1} blue shift upon protonation (Fig. S12) compared to *ca.* 40 cm^{-1} shift observed for **3**. The hydride resonances at δ –11.58 ppm was replaced by two new resonances at and δ –12.39 and –12.42 ppm suggesting that the movement of bridging hydride across the Ru–Ru vectors is retarded upon protonation, a feature also observed for **2** (Scheme 3).

2.4. Electrocatalysis

The proton reduction ability of **1-4** was tested in MeCN using *p*-TsOH·H_2O as the proton source. Since *p*-TsOH·H_2O is reduced by a glassy carbon electrode at *ca.* –1.76 ± 0.15 V [22], CVs of *p*-TsOH·H_2O have also been recorded in absence of catalysts under similar conditions for comparison. CVs of **1** and **2** recorded upon addition of 1-5 molar equivalents are shown in Fig. 8. Cluster **1** displays two new reduction peaks in presence of acid at E_p = –

1.77 V and E_p = –1.94 V in addition to the peak observed for the neutral complex at E_p = –1.61 V (Fig. 8a). The height of all peaks increases with increasing concentration of acid, characteristic of proton reduction. The peak height of the second and third waves increases more rapidly than that of the first wave. In contrast, the CV of **2** shows two new reduction peaks at E_p = –1.24 V and E_p = –1.69 V in presence of acid (Fig. 8b). The peak current of the first wave does not increase with concentration of acid, while that of the second wave increases rapidly with acid concentration indicating reduction of protons by **2** at the latter potential. Although the current from the direct reduction of acid by the glassy carbon electrode is very low for **1**, it contributes significantly to the catalytic limiting current obtained for **2** (Fig. 8).

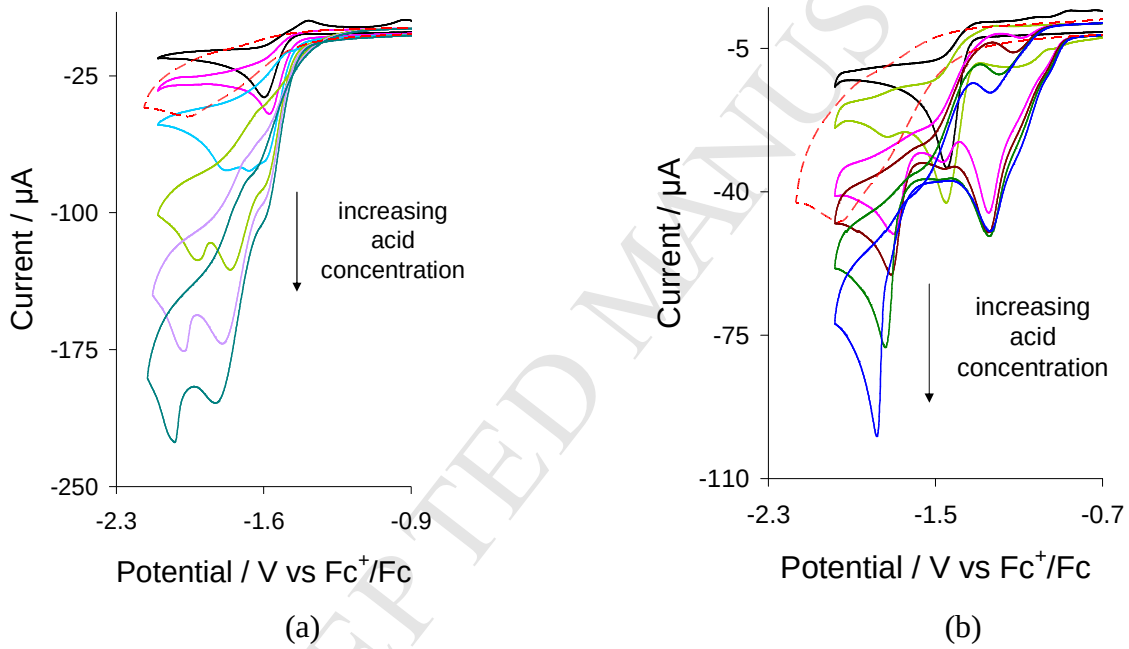

Fig. 8 - CVs of $Fe_3(CO)_9(\mu_3\text{-pyNH})(\mu\text{-H})$ (**1**) (a) and $Fe_3(CO)_9(\mu_3\text{-pymNH})(\mu\text{-H})$ (**2**) (b) in the absence of acid (black) and in the presence of 1-5 equivalents of $TsOH\cdot H_2O$ (in MeCN, 1 mM solution, supporting electrolyte $[NBu_4][PF_6]$, scan rate 0.1 Vs^{-1}, glassy carbon electrode, potential vs Fc^+/Fc). Response of 5 equivalents $TsOH\cdot H_2O$ alone is shown with the red dotted line.

Electrocatalytic data shows that both **1** and **2** can catalyse proton reduction as expected but they follow quite different mechanisms. Since IR results show that **1** is not protonated by $TsOH\cdot H_2O$, it must be reduced before protonation. Three reductive features (catalytic waves) are seen in its CV at E_p = –1.61, –1.77 and –1.94 V in presence of acid (Fig. 8a). The 49-electron radical anion $\mathbf{1}^-$ undergoes rapid protonation to form a neutral dihydride

1H, which releases H_2 and accounts for the catalytic wave observed at the first reduction potential (at E_p = –1.61 V) (Scheme 5). The release of dihydrogen from **1H** is slow and it has time to partially undergo a further reduction (at E_p = –1.77 V) to form 50-electron **1H**$^-$ which then reacts with proton to release H_2 as shown in Scheme 5. The CV of **2** shows two new reduction peaks at E_p = –1.24 and –1.69 V and catalyses proton reduction at the latter potential, its reduction being shifted by ~0.2 V in presence of acid due to protonation at pyrimidine ring nitrogen. Since the neutral hydride can not release H_2 (Fig. 8b), it undergoes a further reduction at E_p = –1.69 V to form **2H**$^-$ which reacts with a second proton before release of H_2 (Scheme 6). Overall, cluster **1** follows both ECEC and ECCE mechanisms, whereas **2** follows only a CEEC mechanism for electrocatalytic proton reduction.

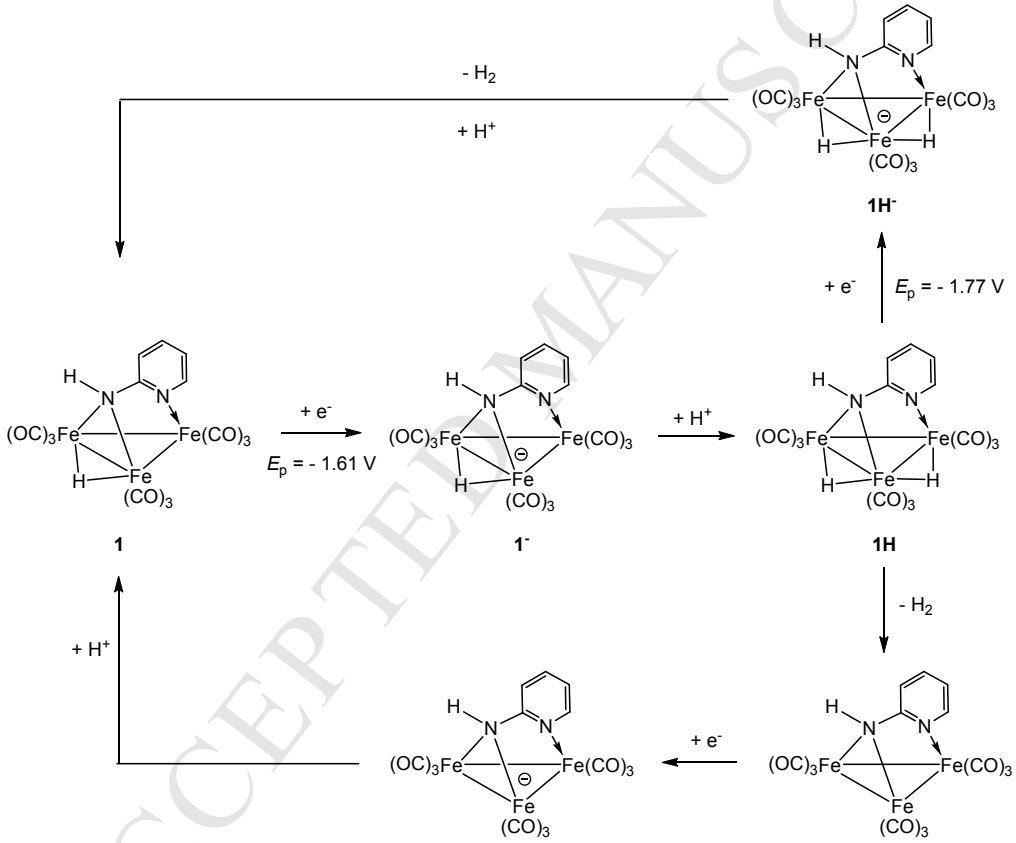

Scheme 5 - Plausible schemes for the electrocatalytic proton reduction by $Fe_3(CO)_9(\mu_3$-pyNH)(μ-H) (**1**).

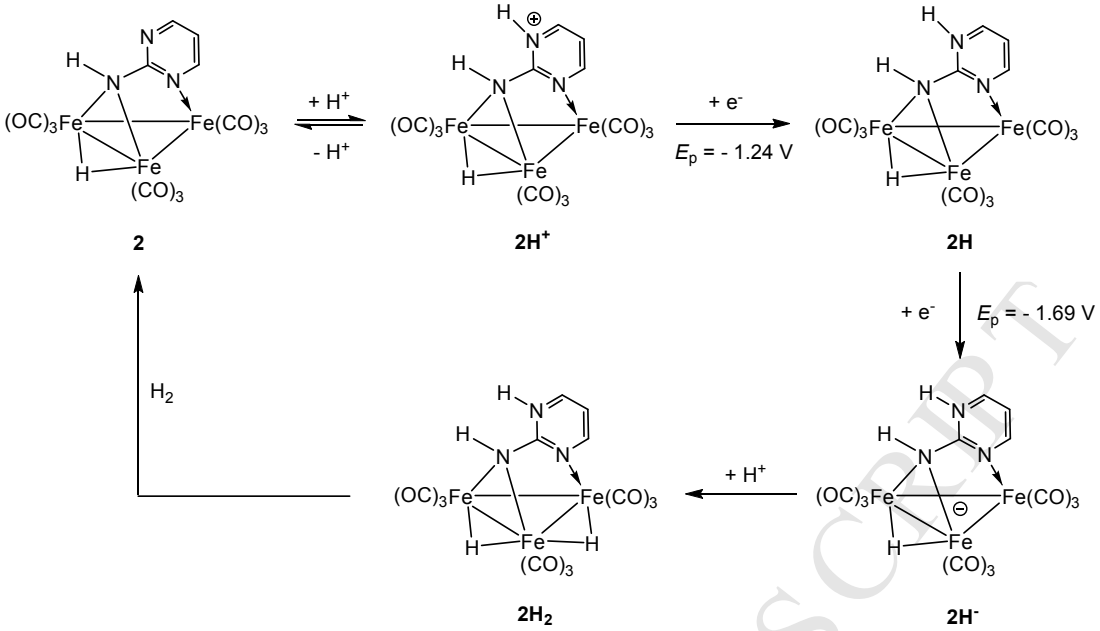

Scheme 6 - Plausible scheme for the electrocatalytic proton reduction by $Fe_3(CO)_9(\mu_3$-pymNH)(μ-H) (**2**).

Fig. 9 shows CVs of **3** and **4** recorded in presence of 1-5 molar equivalents of TsOH·H_2O. Cluster **3** displays a single catalytic wave at its reduction potential (E_p = –2.01 V) due to slow protonation across Ru–Ru vector by TsOH·H_2O (Fig. 9a). Nevertheless, a minor reduction peak has also been observed at E_p = –1.33 V due to the reduction of $\mathbf{3H}^+$ formed in small amounts upon addition of acid. In the proposed mechanism for the electrocatalytic proton reduction by **3** (Scheme 7), catalysis is initiated by reduction of **3** at E_p = –2.01 V. No catalytic event has been seen beyond this potential indicating that release of H_2 from the neutral dihydride **3H** is fast (Scheme 7). This is in contrast with that observed for the triiron cluster **1** whereby the release of H_2 from **1H** is proposed to be relatively slow leading to the development of multiple catalytic waves *via* reduction of **1H**.

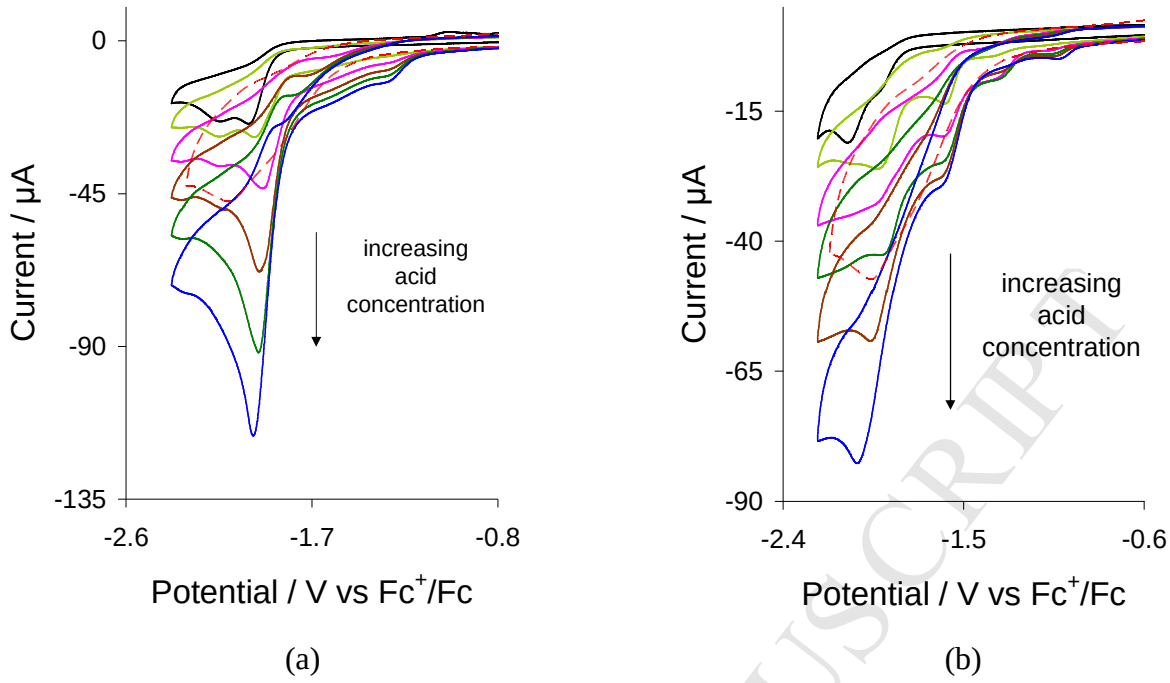

Fig. 9. CVs $Ru_3(CO)_9(\mu_3\text{-pyNH})(\mu\text{-H})$ (**3**) (a) and $Ru_3(CO)_9(\mu_3\text{-pymNH})(\mu\text{-H})$ (**4**) (b) in the absence of acid and in the presence of 1-5 equivalents of $TsOH\cdot H_2O$ (in MeCN, 1 mM solution, supporting electrolyte $[NBu_4][PF_6]$, scan rate 0.1 Vs^{-1}, glassy carbon electrode, potential vs Fc^+/Fc). Response of 5 equivalents $TsOH\cdot H_2O$ alone is shown with the red dotted line.

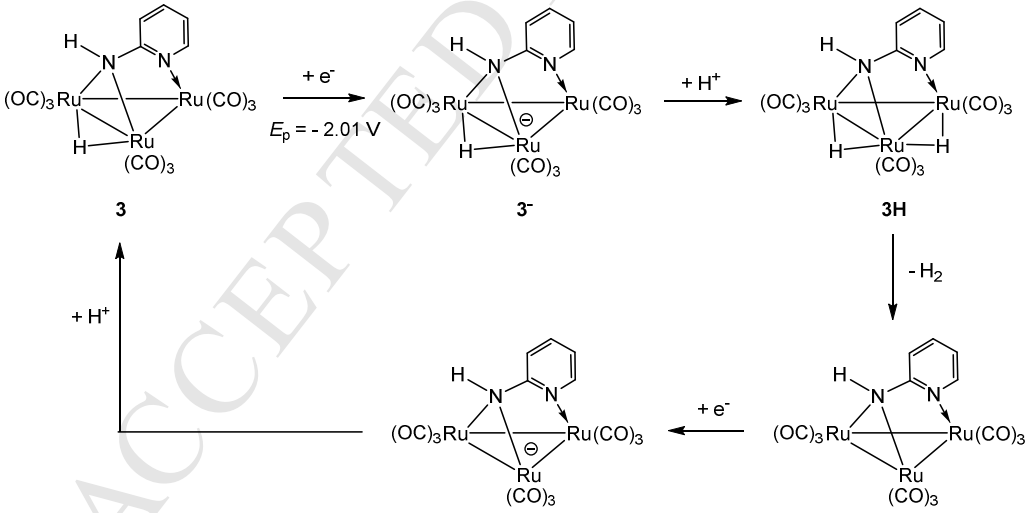

Scheme 7 - Plausible mechanism for the electrocatalytic proton reduction by $Ru_3(CO)_9(\mu_3\text{-pyNH})(\mu\text{-H})$ (**3**).

The CV of **4** exhibits two new reduction peaks at E_p = –1.60 and –1.90 V upon addition of $TsOH\cdot H_2O$ (Fig. 9b). We attribute the first event to the reduction of $\mathbf{4H}^+$ and the latter to the reduction of the generated neutral hydride **4H** (Scheme 8). The peak current of

both waves increases as the concentration of acid is increased, the second wave increasing more rapidly than the first. This is in contrast with the catalysis shown by **2** where there is an increase in peak current only at the second wave. Ruthenium is more electropositive than iron which should make the cluster core of **4H** basic enough for H_2 liberation, unlike **2H** which can not liberate H_2. Release of H_2 from **4H** is relatively slow thereby competing with the reduction at E_p = –1.90 V to form $\mathbf{4H}^-$ (Scheme 8). We then proposed that the latter reacts with a proton to form $\mathbf{4H}_2$ which releases H_2 and regenerates the catalyst (Scheme 8). However, the direct reduction of $TsOH \cdot H_2O$ at the electrode contributes significantly (*ca.* 30 and 50% of the total catalytic limiting current obtained for **3** and **4** respectively) during catalysis by these triruthenium clusters (Fig. 9) as compared to their triiron analogues (Fig. 8). To minimize direct reduction of acid at the electrode, we have also used the relatively weak acid CF_3CO_2H ($pK_a \approx 12.7$ in MeCN)[21] as the proton source, but all these clusters do not show significant catalytic activity in the presence of CF_3CO_2H.

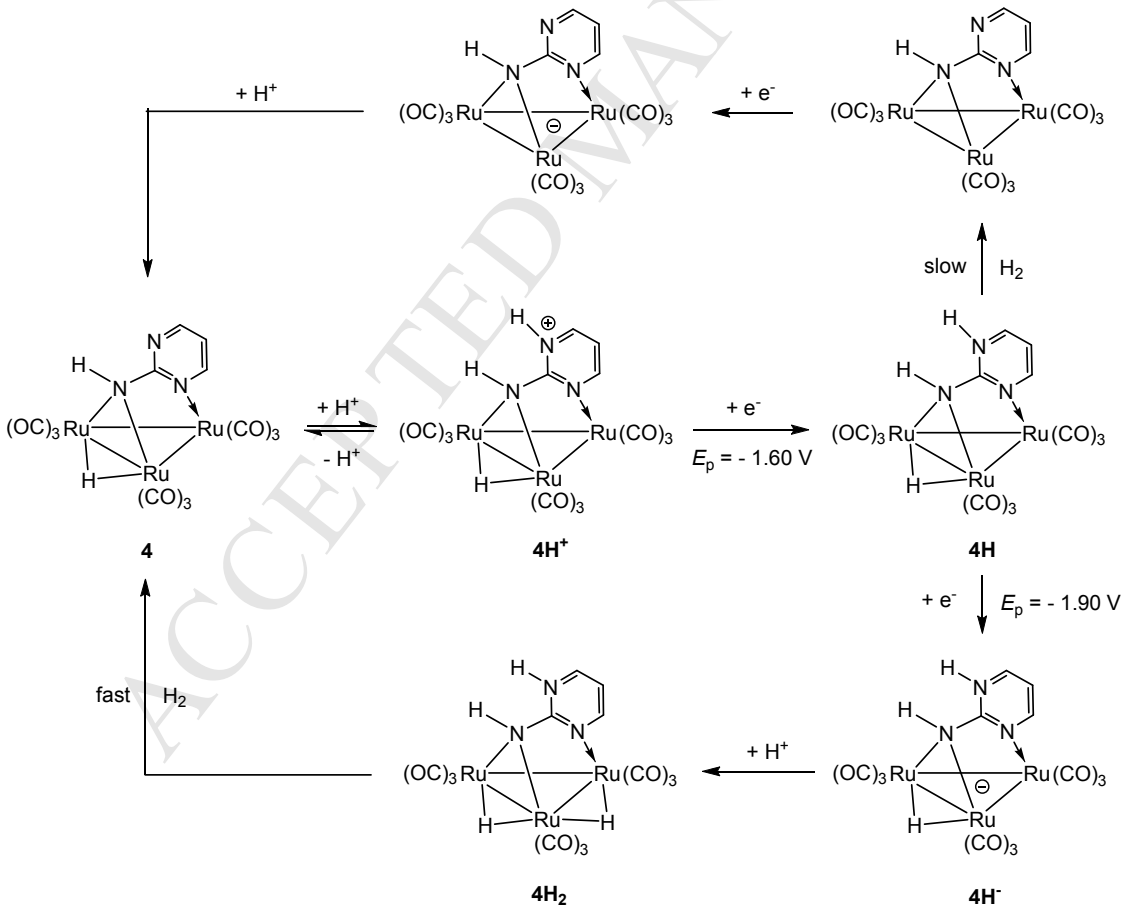

Scheme 8 - Proposed mechanisms for the electrocatalytic proton reduction by $Ru_3(CO)_9(\mu_3\text{-pymNH})(\mu\text{-H})$ (**4**).

Since the current from the direct reduction of $TsOH \cdot H_2O$ by the electrode is insignificant as compared to the total catalytic limiting current obtained for **1**, we have used these limiting currents to measure its catalytic efficiency. A plot of catalytic current/non-catalytic current ratio (i_{cat}/i_p) *vs* acid concentration for the first and second catalytic waves of **1** is shown in Fig. 10. The i_{cat}/i_p value approaches 7 after addition of 10 equivalents of $TsOH \cdot H_2O$ for the first catalytic wave (at E_p = –1.61 V), while the ratio increases to a maximum value of 4 for the second wave (at E_p = *ca.* –1.80 V) after addition of 8 equivalents of acid. Although a large number of biomimetic diiron systems were developed as models of the active site of [FeFe]-hydrogenases over the past two decades, no biomimetic diiron catalyst has been found to show high i_{cat}/i_p values (> 3) at reasonable potentials [12b]. Proton reduction catalysts based on a single iron exhibit better i_{cat}/i_p ratio (~ 4 to 10) as compared to the diiron systems. The highest i_{cat}/i_p value of 38 has been shown by a nickel complex namely $[(P^{Ph}{}_2N^{Ph})_2Ni]^{2+}$ ($P^{Ph}{}_2N^{Ph}$ = 1,3,6-triphenyl-1-aza-3,6-diphosphacycloheptane) [23] reported by DuBois. We have also plotted i_{cat}/i_p against acid concentration for **2**-**4** (Fig. S13), but we opted not to discuss these data since direct reduction of $TsOH \cdot H_2O$ at the electrode contributes significantly at their (especially **4**) catalytic potentials.

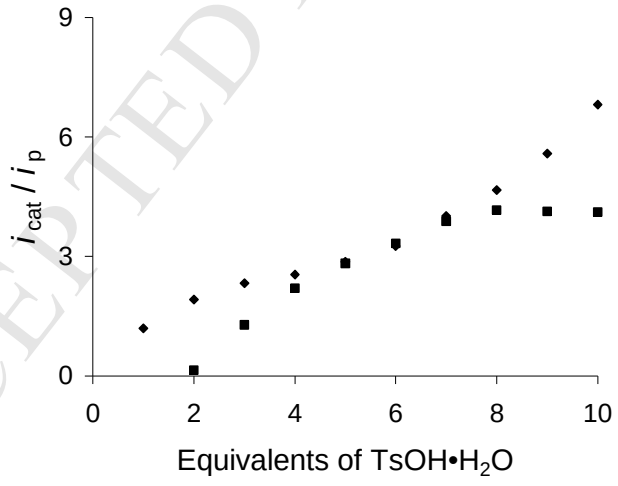

Fig. 10. Dependence of i_{cat}/i_p on $TsOH \cdot H_2O$ concentration for $Fe_3(CO)_9(\mu_3\text{-pyNH})(\mu\text{-H})$ (**1**) - at potentials of the first (black diamonds) and second (black squares) reduction waves (1 m*M* solution in acetonitrile, 1-10 equivalents $TsOH \cdot H_2O$, supporting electrolyte $[NBu_4][PF_6]$, scan rate 0.1 Vs^{-1}, glassy carbon electrode).

3. Conclusions

The proton reduction ability of triiron and triruthenium clusters containing acidic and hydridic hydrogens in close proximity (*ca.* 2.8Å) has been investigated under electrochemical conditions. The electrochemical response of these clusters is sensitive to the nature of the heterocyclic amine which can be easily tuned by modifying the latter. All catalyze proton reduction in the presence of $TsOH \cdot H_2O$, but follow different mechanisms. Electrocatalytic data also indicate that the residual amino (acidic) hydrogen of 2-aminopyridinate clusters does not take part in H_2 generation, whereas that of the 2-aminopyrimidinate cluster **4** may be involved in the production of H_2.

Analysis of catalytic limiting currents suggest that the triiron clusters are better catalysts than their triruthenium analogues, and the presence of a proton relay neither increases the efficiency nor reduces the overpotential of catalysis. The triiron clusters also operate at reduced overpotentials as compared to the triruthenium models. Further studies which involve substitution of one or more carbonyls by basic phosphines to facilitate rapid protonation across metal-metal bond, as well as use of more electron withdrawing 2-aminopyridines to reduce the overpotential of the catalytic process, are ongoing in our laboratory and will be reported elsewhere.

4. Experimental Section

4.1. General

Unless otherwise stated, all manipulations were carried out under a nitrogen atmosphere using standard Schlenk techniques. Reagent-grade solvents were dried using appropriate drying agents and distilled prior to use by standard methods. Infrared spectra were recorded using a Nicolet 6700 FT-IR spectrometer in a solution cell fitted with calcium fluoride plates, subtraction of the solvent absorptions being achieved by computation. NMR spectra were run on a Bruker AMX400 instrument. All chemical shifts are reported in δ units with reference to the residual protons of the deuterated solvents for proton. Preparative thin layer chromatography (TLC) was carried out on 0.25 mm plates prepared from silica gel GHLF (UV254, Analtech). Carbonyl clusters were purchased from Alfa Aesar (A Johnson

Matthey Company) and used without further purification. 2-Aminopyridinate ($pyNH_2$) and 2-aminopyrimidinate ($pymNH_2$) were purchased from Sigma-Aldrich and used as received. Clusters **3** and **4** were prepared according to published procedures [18b-c].

*4.2. Synthesis of $Fe_3(CO)_9(\mu_3$-pyNH)(μ-H) (**1**)*

To a benzene (20 mL) solution of $Fe_3(CO)_{12}$ (500 mg, 0.993 mmol) was added $pyNH_2$ (190 mg, 1.997 mmol) and the mixture was then heated to reflux for 1 h. The solvent was removed under vacuum and the residue separated by chromatography on TLC plates. Elution with hexane/CH_2Cl_2/MeCN (5:5:1, v/v) developed four bands on TLC plate. The first and fourth bands were unconsumed $Fe_3(CO)_{12}$ (trace) and $pyNH_2$ (trace) respectively. The third band afforded $Fe_3(CO)_9(\mu_3$-pyNH)(μ-H) (**1**) (21 mg, 4%) as red crystals after recrystallization from hexane/CH_2Cl_2 at 4 °C. The contents of the second band were two small for characterisation. Data for **1**: IR (νCO, CH_2Cl_2): 2071m, 2032vs, 2010vs, 1981s, 1973sh cm^{-1}. ^{1}H NMR ($CDCl_3$): δ 8.26 (m, 1H), 7.39 (m, 1H), 6.82 (m, 1H), 6.61 (m, 1H), 3.55 (br, s, 1H), –12.66 (s, 1H). Elemental analysis calc. for $C_{14}H_6Fe_3N_2$ (found): C 33.73 (33.62), H 1.17 (1.26), N 5.45 (5.51).

*4.3. Synthesis of $Fe_3(CO)_9(\mu_3$-pymNH)(μ-H) (**2**)*

A benzene (20 mL) solution of $Fe_3(CO)_{12}$ (500 mg, 0.993 mmol) and $pymNH_2$ (190 mg, 1.998 mmol) was heated to reflux for 1 h. The solvent was removed under reduced pressure and the residue chromatographed by TLC on silica gel. Elution with hexane/CH_2Cl_2 (1:1, v/v) developed two bands on the TLC plates. The first band afforded $Fe_3(CO)_9(\mu_3$-pymNH)(μ-H) (**2**) (40 mg, 8%) as red crystals after recrystallization from hexane/CH_2Cl_2 at 4 °C. The second band was unconsumed $pymNH_2$ (trace). Data for **2**: IR (νCO, CH_2Cl_2): 2074m, 2036vs, 2013vs, 1992s, 1975sh cm^{-1}. ^{1}H NMR ($CDCl_3$): δ 8.54 (dd, J 5.0, 2.2, 1H), 8.18 (dd, J 5.0, 2.2, 1H), 6.82 (t, J 5.0, 1H), 3.68 (br, s, 1H), –12.65 (s, 1H). Elemental analysis calc. for $C_{13}H_5Fe_3N_2$ (found): C 30.33 (30.82), H 0.98 (1.03), N 8.17 (8.24).

*4.4. Synthesis of $Ru_3(CO)_9(\mu_3$-pyNH)(μ-H) (**3**)*

To a toluene (20 mL) solution of $Ru_3(CO)_{12}$ (100 mg, 0.156 mmol) was added $pyNH_2$ (30 mg, 0.319 mmol) and the mixture was then heated to reflux for 90 min. The reaction

mixture was then allowed to cool at room temperature and pass through a short column (1 cm) made of silica (0.5 cm) and celite (0.5 cm) with the latter on top. The volatiles from the filtrate were removed by rotary evaporation and the residue re-dissolved in minimum amount of CH_2Cl_2 (3 mL). A layer of hexane was poured over this solution which was then left standing at room temperature for crystallization. $Ru_3(CO)_9(\mu_3\text{-pyNH})(\mu\text{-H})$ (**3**) (34 mg, 33%) was obtained as orange crystals from this solution after several days. Data for **3**: IR (νCO, CH_2Cl_2): 2081m, 2050vs, 2027vs, 1995vs, 1964w cm^{-1}. ^1H NMR ($CDCl_3$): δ 8.15 (dd, J 8.0, 4.0, 1H), 7.44 (m, 1H), 6.77 (m, 1H), 6.57 (d, J 8.0, 1H), 4.46 (br, s, 1H), –11.39 (s, 1H). Elemental analysis calc. for $C_{14}H_6N_2O_9Ru_3$ (found): C 25.89 (26.61), H 0.93(1.01), N 4.31 (4.34).

*4.5. Synthesis of $Ru_3(CO)_9(\mu_3$-pymNH)(μ-H) (**4**)*

A toluene (20 mL) solution of $Ru_3(CO)_{12}$ (100 mg, 0.156 mmol) and $pymNH_2$ (30 mg, 0.315 mmol) was heated to reflux for 90 min. A similar work up described above afforded $Ru_3(CO)_9(\mu_3\text{-pymNH})(\mu\text{-H})$ (**4**) (42 mg, 41%) as orange crystals. Data for **4**: IR (νCO, CH_2Cl_2): 2084m, 2055vs, 2031vs, 2000vs, 1965w cm^{-1}. ^1H NMR ($CDCl_3$): δ 8.42 (dd, J 8.0, 4.0, 1H), 8.20 (dd, J 8.0, 4.0, 1H), 6.76 (t, J 8.0, 1H), 4.55 (br, s, 1H), –11.38 (s, 1H). Elemental analysis calc. for $C_{13}H_5N_3O_9Ru_3$ (found): C 24.00 (24.47), H 0.77 (0.81), N 6.46 (6.53).

4.6. Electrochemical Studies

Electrochemistry was carried out in deoxygenated MeCN with 0.1 M $TBAPF_6$ as the supporting electrolyte. The working electrode was a 3 mm diameter glassy carbon electrode that was polished with 0.3 μm alumina slurry prior to each scan. The counter electrode was a Pt wire and the quasi-reference electrode was a silver wire. All CVs were referenced to the Fc^+/Fc redox couple. An Autolab potentiostat (EcoChemie, Netherlands) was used for all electrochemical measurements. Catalysis studies were carried out by adding equivalents of $TsOH\cdot H_2O$ (Sigma-Aldrich).

4.7. X-ray Structure Determination

Single crystals of **2**-**4** suitable for X-ray diffraction were mounted on glass fibres and all geometric and intensity data were taken from these samples using a Bruker SMART APEX CCD diffractometer using graphite-monochromated Mo-Kα radiation (λ = 0.71073 Å) at 150 ± 2 K. Data collection, indexing and initial cell refinements were all done using SMART [24] software. Data reduction were carried out with SAINT PLUS [25] and absorption corrections applied using the programme SADABS [26]. Structures were solved by direct methods and developed using alternating cycles of least-squares refinement and difference-Fourier synthesis. All non-hydrogen atoms were refined anisotropically. All hydrogen atoms of **2** and the bridging hydride of **3** and **4** were located from Fourier maps, while all other hydrogen atoms of **3** and **4** were included using a riding model. Structure solution used SHELXTL PLUS V6.10 program package [27].

Crystallographic data for **2**: red block, dimensions 0.44 × 0.42 × 0.36 mm^3, monoclinic, space group $P2_1/n$, a = 10.639(3), b = 11.114(3), c = 14.553(4) Å, α = 90, β = 102.534(4), γ = 90°, V = 1679.8(8) $Å^3$, Z = 4, F(000) 1016, d_{calc} = 2.035 g cm^{-3}, μ = 2.613 mm^{-1}. 13520 reflections were collected, 3922 unique [R(int) = 0.0400] of which 3019 were observed [$I > 2.0\sigma(I)$]. At convergence, R_1 = 0.0308, wR_2 = 0.0665 [$I > 2.0\sigma(I)$] and R_1 = 0.0418, wR_2 = 0.0678 (all data), for 273 parameters. Crystallographic data for **3**: orange block, dimensions 0.40 × 0.20 × 0.16 mm^3, monoclinic, space group $P2_1/c$, a = 10.020(2), b = 15.737(4), c = 11.524(3) Å, α = 90, β = 97.259(4), γ = 90°, V = 1802.7(7) $Å^3$, Z = 4, F(000) 1232, d_{calc} = 2.393 g cm^{-3}, μ = 2.533 mm^{-1}. 14158 reflections were collected, 4113 unique [R(int) = 0.0307] of which 3401 were observed [$I > 2.0\sigma(I)$]. At convergence, R_1 = 0.0214, wR_2 = 0.0424 [$I > 2.0\sigma(I)$] and R_1 = 0.0289, wR_2 = 0.0432 (all data), for 277 parameters. Crystallographic data for **4**: orange block, dimensions 0.46 × 0.44 × 0.40 mm^3, monoclinic, space group $P2_1/n$, a = 10.751(2), b = 11.279(2), c = 15.009(3) Å, α = 90, β = 102.088(3), γ = 90°, V = 1779.6(5) $Å^3$, Z = 4, F(000) 1232, d_{calc} = 2.428 g cm^{-3}, μ = 2.568 mm^{-1}. 13869 reflections were collected, 4082 unique [R(int) = 0.0343] of which 3614 were observed [$I > 2.0\sigma(I)$]. At convergence, R_1 = 0.0221, wR_2 = 0.0518 [$I > 2.0\sigma(I)$] and R_1 = 0.0260, wR_2 = 0.0527 (all data), for 274 parameters.

Appendix A. Supplementary Information

Additional electrochemical and spectroscopic information are given in Figs. S1-S13. CCDC 1410468 (for **2**), CCDC 1413990 (for **3**) and CCDC 1413991 (for **4**) contain supplementary crystallographic data. These data may be obtained free of charge from The Cambridge Crystallographic Data Center via www.ccdc.cam.ac.uk/data_request/cif.

Acknowledgements

We thank the Commonwealth Scholarship Commission for the award of a Commonwealth Scholarship to S.G. and King's College London for funding.

References

[1] For some reviews of this area see:
(a) I.P. Georgakaki, L.M. Thomson, E.J. Lyon, M. B. Hall, M.Y. Darensbourg, Coord. Chem. Rev. 238-239 (2003) 255-266;
(b) D.J. Evans, C.J. Pickett, Chem. Soc. Rev. 32 (2003) 268-287;
(c) T.B. Rauchfuss, Inorg. Chem. 43 (2004) 14-26;
(d) L. Sun, B. Åkermark, S. Ott, Coord. Chem. Rev. 249 (2005) 1653-1663;
(e) X. Liu, S. K. Ibrahim, C. Tard, C.J. Pickett, Coord. Chem. Rev. 249 (2005) 1641-1652;
(f) J.-F. Capon, F. Gloaguen, P. Schollhammer, J. Talarmin, Coord. Chem. Rev. 249 (2005) 1664-1676.

[2] (a) S. Ghosh, G. Hogarth, N. Hollingsworth, K.B. Holt, I. Richard, M.G. Richmond, B. Sanchez, D. Unwin, Dalton Trans. 42 (2013) 6775–6792;
(b) F. Ridley, S. Ghosh, G. Hogarth, N. Hollingsworth, K.B. Holt, D. Unwin, J. Electroanal. Chem. 703 (2013) 14–22;
(c) S. Ghosh, G. Hogarth, N. Hollingsworth, K.B. Holt, S.E. Kabir, B. Sanchez, Chem. Commun. 50 (2014) 945–947.

[3] (a) M.H. Cheah, C. Tard, S.J. Borg, X. Liu, S.K. Ibrahim, C.J. Pickett, S.P. Best, J. Am. Chem. Soc. 129 (2007) 11085-11092;
(b) C. Tard, X. Liu, D.L. Hughes, C.J. Pickett, Chem. Commun. (2005) 133-135.

[4] (a) S. Ghosh, G. Hogarth, K.B. Holt, S.E. Kabir, A. Rahaman, D.G. Unwin, Chem. Commun. 47 (2011) 11222-11224;

(b) A. Rahaman, S. Ghosh, D.G. Unwin, S. Basak- Modi, K.B. Holt, S.E. Kabir, E. Nordlander, M.G. Richmond, G. Hogarth, Organometallics 33 (2014) 1356-1366.

[5] J. Yeo, M.H. Cheah, M.I. Bondin, S.P. Best, Aust. J. Chem. 65 (2012) 241-253.

[6] Z. Li, X. Zeng, Z. Niu, X. Liu, Electrochimica Acta 54 (2009) 3638-3644.

[7] C.A. Mebi, K.E. Brigance, R.B. Bowman, J. Braz. Chem. Soc. 23 (2012) 186-189.

[8] W. Gao, J. Sun, M. Li, T. Åkermark, K. Romare, L. Sun, B. Åkermark, Eur. J. Inorg. Chem. (2011) 1100-1105.

[9] M.D. Rail, L.A. Berben, J. Am. Chem. Soc. 133 (2011) 18577-18579.

[10] A.D. Nguyen, M.D. Rail, M. Shanmugam, J.C. Fettinger, L.A. Berben, Inorg. Chem. 52 (2013) 12847-12854.

[11] S. Ghosh, K.B. Holt, S.E. Kabir, M.G. Richmond, G. Hogarth, Dalton Trans. 44 (2015) 5160-5169.

[12] (a) I. Bhugun, D. Lexa, J.-M. Saveánt, J. Am. Chem. Soc. 118 (1996) 3982-3983;
(b) M.J. Rose, H.B. Gray, J.R. Winkler, J. Am. Chem. Soc. 134 (2012) 8310-8313;
(c) V. Artero, M. Fontecave, C. R. Chimie 11 (2008) 926-931.

[13] (a) S. Kaur-Ghumaan, L. Schwartz, R. Lomoth, M. Stein, S. Ott, Angew. Chem. Int. Ed. 49 (2010) 8033-8036;
(b) M. Beyler, S. Ezzaher, M. Karnahl, M.-P. Santoni, R. Lomoth, S. Ott, Chem. Commun. 47 (2011) 11662-11664;
(c) A. Orthaber, M. Karnahl, S. Tschierlei, D. Streich, M. Stein, S. Ott, Dalton Trans. 43 (2014) 4537-4549.

[14] (a) S. Roy, S.K.S. Mazinani, T. L. Groy, L. Gan, P. Tarakeshwar, V. Mujica, A.K. Jones, Inorg. Chem. 53 (2014) 8919-8929;
(b) G.P. Connor, K.J. Mayer, C.S. Tribble, W.R. McNamara, Inorg. Chem. 53 (2014) 5408-5410.

[15] (a) A.J. Cornish, K. Gärtner, H. Yang, J.W. Peters, E.L. Hegg, J. Biol. Chem. 286 (2011) 38341-38347;
(b) B.E. Schultz, S.I. Chan, Annu. Rev. Biophys. Biomol. Struct. 30 (2001) 23-65;
(c) S. Cukierman, Biochim. Biophys. Acta 1757 (2006) 876-885;
(d) S.J. Whitehead, M. Iwaki, N.P. Cotton, P.R. Rich, J.B. Jackson, Biochim. Biophys. Acta 1787 (2009) 1276-1288.

[16] H.J. Fan, M.B. Hall, J. Am. Chem. Soc. 123 (2001) 3828-3829.

[17] C. Greco, M. Bruschi, L.D. Gioia, U. Ryde, Inorg. Chem. 46 (2007) 5911-5921.

[18] (a) J.A. Cabeza, Eur. J. Inorg. Chem. (2002) 1559-1570;

(b) J.A. Cabeza, I. del Río, M. Moreno, S. García-Granda, M. Pérez-Priede, V. Riera, Eur. J. Inorg. Chem. (2002) 3204-3209;

(c) P.L. Andreu, J.A. Cabeza, V. Riera, J. Chem. Soc., Dalton Trans. (1990) 2201-2206;

(d) P.L. Andreu, J.A. Cabeza, V. Riera, C. Bois, Y. Jeannin, J. Organomet. Chem. 384 (1990) C25-C28;

(e) P.L. Andreu, J.A. Cabeza, V. Riera, J. Chem. Soc., Dalton Trans. (1990) 3347-3353.

[19] (a) P.L. Andreu, J.A. Cabeza, M.A. Pellinghelli, V. Riera, Inorg. Chem. 30 (1991) 4611-4616;

(b) P.L. Andreu, J.A. Cabeza, J.L. Cuyás, V. Riera, J. Organomet. Chem. 427 (1992) 363-368;

(c) J.A. Cabeza, I. del Río, P. García-Álvarez, D. Miguel, Can. J. Chem. 84 (2006) 105-110;

(d) J.A. Cabeza, I. del Río, S. García-Granda, L. Martínez-Méndez, M. Moreno, V. Riera, Organometallics 22 (2003) 1164-1166;

(e) J.A. Cabeza, I. del Río, S. García-Granda, M. Moreno, E. Pérez-Carreño, M. Suárez, Organometallics 23 (2004) 5849-5855.

[20] B.F.G. Johnson, A. Rodgers, in '*The Chemistry of Metal Cluster Complexes*', Eds. D.F. Shriver, H.D. Kaesz, R.D. Adams, (1990) 303-325.

[21] K. Izutsu, in '*Acid-Base Dissociation Constants in Dipolar Aprotic Solvents*', Blackwell Scientific Publications, Oxford, (1990).

[22] B.D. McCarthy, D.J. Martin, E.S. Rountree, A.C. Ullman, J.L. Dempsey, Inorg. Chem. 53 (2014) 8350-8361.

[23] M.L. Helm, M.P. Stewart, R.M. Bullock, M.R. DuBois, D.L. DuBois, Science 333 (2011) 863-866.

[24] SMART Version 5.628; Bruker AXS, Inc., 5465 East Cheryl Parkway, Madison, WI 53711-5373, (2003).

[25] SAINT Version 6.36A; Bruker AXS, Inc., 5465 East Cheryl Parkway, Madison, WI 53711-5373, (2002).

[26] G.M. Sheldrick, SADABS Version 2.10; University of Göttingen, Göttingen, Germany, (2003).

[27] G.M. Sheldrick, A short history of SHELX. Acta Crystallogr. A64 (2008) 112-122.

Highlights for review

- Synthesis of a triiron and triruthenium 2-aminopyridinate/pyrimidinate clusters
- Crystal structures and protonation studies
- Electrocatalysts for the hydrogen evolution reaction (HER)